JOURNAL OF GEOPHYSICAL RESEARCH, VOL. 112, A11314, doi:10.1029/2007JA012327, 2007

A method for determining the drift velocity of plasma depletions in the equatorial ionosphere using far-ultraviolet spacecraft observations

S. H. Park,[1] S. L. England,[1] T. J. Immel,[1] H. U. Frey,[1] and S. B. Mende[1]

Received 7 February 2007; revised 12 June 2007; accepted 25 July 2007; published 27 November 2007.

[1] The Far-Ultraviolet Imager (IMAGE-FUV) on board the NASA IMAGE satellite has been used to observe plasma depletions in the nightside equatorial ionosphere. Observations from periods around spacecraft apogee, during which equatorial regions are visible for several hours, have allowed the velocity of these plasma depletions to be determined. A new method for determining the velocity of these depletions using an image analysis technique, Tracking Of Airglow Depletions (TOAD), has been developed. TOAD allows the objective identification and tracking of depletions. The automation of this process has also allowed for the tracking of a greater number of depletions than previously achieved without requiring any human input, which shows that TOAD is suitable for use with large data sets and for future routine monitoring of the ionosphere from space. Furthermore, this automation allows the drift velocities of each bubble to be determined as a function of magnetic latitude, which will give us the capability of retrieving geophysically important parameters such as the electric field, which are believed to vary rapidly with magnetic latitude.

Citation: Park, S. H., S. L. England, T. J. Immel, H. U. Frey, and S. B. Mende (2007), A method for determining the drift velocity of plasma depletions in the equatorial ionosphere using far-ultraviolet spacecraft observations, *J. Geophys. Res.*, *112*, A11314, doi:10.1029/2007JA012327.

1. Introduction

[2] Global-scale observations of nighttime-ionospheric airglow have been obtained using the IMAGE Far-Ultraviolet Imager (IMAGE-FUV) [*Mende et al.*, 2000a, 2000b] and the TIMED Global Ultraviolet Imager (GUVI) [*Humm et al.*, 1998; *Paxton et al.*, 1999; *Christensen et al.*, 2003]. Both instruments measure nighttime 135.6-nm emissions from OI. The brightness of these emissions at night corresponds to the line-of-sight integrated product of the O^+ and e^- number densities and hence are highly sensitive to changes in plasma density (see *Meier* [1991] for a detailed discussion). These emissions come from a range of altitudes, with the brightest at low latitudes coming from 300 to 450 km [see *Henderson et al.*, 2005b, Figure 2].

[3] Recently, the large-scale structure of the equatorial airglow arcs has been characterized using these nighttime IMAGE-FUV and GUVI observations [*Sagawa et al.*, 2003, 2005; *Henderson et al.*, 2005a; *Immel et al.*, 2006; *England et al.*, 2006a, 2006b]. These authors have demonstrated that the mean structure of the nighttime ionosphere can be determined throughout most of the evening under favorable conditions. The brightness of the 135.6 nm-airglow arcs is strongly dependent upon the solar UV flux. Partly for this reason, these studies have primarily focused on data obtained from 2002 (data from 2003 is also included in the work of *Henderson et al.* [2005a]), which was close to solar maximum.

[4] Using these nighttime airglow observations, it has also been possible to observe plasma density depletions associated with plasma bubbles and equatorial spread *F*. GUVI has been used to study the occurrence rates of such depletions for different seasons and local times [*Henderson et al.*, 2005a]. However, the orbit of the TIMED satellite only permits GUVI to observe any one depletion for a brief amount of time and thus GUVI is unsuitable for the determination of the drift velocity of such depletions. The high apogee orbit of the IMAGE satellite allows for extended periods of observation of the nighttime ionosphere that can last for several hours. *Immel et al.* [2003] have presented a method to use these continuous observational periods to determine the drift velocity of the low-latitude plasma depletions.

[5] This method was used by the authors to compare the globally averaged zonal drift velocity of plasma depletions observed by IMAGE-FUV with the average plasma drift velocity measured by the Jicamarca incoherent scatter radar presented by *Fejer et al.* [1991]. This comparison showed a good agreement of the measured velocities as a function of magnetic local time (MLT), but the plasma depletion drift velocities observed by IMAGE-FUV were 10–50 ms^{-1} higher than the average plasma drift velocities recorded by Jicamarca, with the largest differences at early MLT. The authors attributed these differences to a latitudinal shear in zonal drifts but were unable to measure the size of such a

[1]Space Sciences Laboratory, University of California, Berkeley, California, USA.

0148-0227/07/2007JA012327$09.00

shear using their technique. *Lin et al.* [2005] compared the drift velocities observed by IMAGE-FUV with in situ plasma drift velocity and plasma density measurements made by the Ionospheric Plasma and Electrodynamics Instrument (IPEI) instrument on board ROCSAT-1. The authors found that the plasma depletion drift velocities were higher than the background plasma drift by 30–200 ms^{-1}. The authors attributed this difference to coupling between the plasma depletion and an acoustic gravity wave mode which they identified in their in situ observations. This result shows that the drift speed of the plasma depletions observed by IMAGE-FUV may not necessarily be simply explained by the background plasma drift. As plasma depletions have important implications for radio wave propagation such as those used by GPS systems, further study of their propagation characteristics is both timely and important to the broader scientific community.

[6] *Immel et al.* [2004] used the method of *Immel et al.* [2003] to perform the most comprehensive study to date of the statistical properties of the zonal drift speeds of plasma depletions observed by IMAGE-FUV. Focusing on the period of March–May 2002, the authors investigated the dependence of these drift velocities on magnetic longitude (MLon), K_p, D_{st}, F10.7, and solar EUV flux. They demonstrated a strong dependence of the observed drift speeds of plasma depletions on D_{st}, that they attributed to penetrating ring current electric fields. They also found a longitudinal dependence with a peak in plasma depletion drift velocities around the Indian sector, that they attributed to a possible variation in the dynamo electric fields. However, it is worth stating here that the method of *Immel et al.* [2003] relies on human input and thus is somewhat subjectively selective. Time constraints on this human input have meant that this method was severely limited in the number of depletions that could be tracked (*Immel et al.* [2003, 2004] considered only 94 plasma depletions in their studies). These same time constraints also meant that the IMAGE-FUV observations were averaged across 0–25° magnetic latitude (MLat), and thus estimates of the latitudinal shear of these drifts, that is essential to furthering our understanding of the statistical variability of the parameters which drift the zonal drift.

[7] Here we present an improved, fully automated and objective image analysis technique, hereafter referred to as the Tracking Of Airglow Depletions (TOAD) method, for retrieving plasma depletion drift velocities from high-apogee spacecraft airglow observations, such as those from IMAGE-FUV. In processing the data analyzed by *Immel et al.* [2003], TOAD determined the zonal drift velocity for around twice as many depletions, without requiring any human input. These characteristics mean that TOAD is more suitable than the method used previously for statistical surveys of large data sets or possible future routine monitoring of the ionosphere. Significantly, TOAD is also able to determine the drift velocity of plasma depletions across the 0–25° MLat range at 0.5° intervals using IMAGE-FUV quality images (a process that would have increased the human input time by a factor of 50 using the previous method). It is worth noting here that TOAD has not been developed to study the depletion occurrence rates but rather only the locations and drift velocities of the depletions that it identifies. In section 2, we shall briefly summarize the method of *Immel et al.* [2003]. Section 3 will detail our image analysis technique and results for the example of 25–26 April 2002. This was a magnetically quiet period (the 3-h planetary K_p index was 2 or less for the previous 36 h), with moderately high solar EUV flux (F10.7 cm flux = $167 \times 10^{-22} Js^{-1}m^{-2}Hz - 1$), which has been demonstrated to be ideal for IMAGE-FUV observations of the equatorial airglow arcs [e.g., *Immel et al.*, 2006]. In section 4, we shall compare the velocities determined by TOAD to those determined manually by *Immel et al.* [2003] for both this same observational period and for the further example of 7 May 2002.

2. Previous IMAGE-FUV Analysis

[8] The analysis of IMAGE-FUV images to determine the drift velocities of plasma depletions that was used in the studies described in section 1 has been presented in detail by *Immel et al.* [2003]. Therefore this section will only provide a brief summary of this technique, highlighting the points that are required for the comparison between the two methods given in section 4.

[9] During March–May 2002, IMAGE-FUV was able to clearly observe the nighttime emissions of the northern equatorial airglow arc during almost every orbit of the spacecraft. Figure 1 shows the mean of 36 minutes of observations (19 consecutive images) from close to apogee for 25 April 2002, when mapped onto the globe. The bright emissions on the left edge of the left projection and the top of the right projection are OI dayglow emissions, which do not represent ionospheric structure. Away from this region, both northern and southern airglow arcs and the depletions embedded within them are clearly visible. In this case, these can be seen throughout most of the evening-time observations.

[10] While there is a notable change in the MLat of the airglow arcs with longitude during magnetically quiet periods [e.g., *Immel et al.*, 2006], the brightest nighttime 135.6 nm airglow emissions in the northern hemisphere are essentially always found within the 0–25° MLat region. In order to highlight the plasma depletions within these arcs, *Immel et al.* [2003] first mapped each individual image obtained from FUV into APEX magnetic coordinates [*Richmond*, 1995] with 0.5° MLon resolution and then summed all instrument counts over this magnetic latitude range. Implicit within this step is the assumption that any latitudinal shear must be small compared to the width and duration of the depletions. In order to track the drift velocity of the depletions, several hours of images were processed in this way and a keogram of these summed instrument counts was produced. Figure 2 shows the keogram corresponding to the same orbit as the data in Figure 1. The plasma depletions which were visible in the snapshot in Figure 1 can be seen to move eastward with UT in this keogram. Using these keograms, *Immel et al.* [2003] were able to manually track the location of the depletion as a function of UT. They recorded the position each depletion at 15 UT positions and then performed a least squares fit to these positions using a first- through fourth-order polynomial and selected the best using a chi-squared test for the fit of each respective order. They repeated this processes twice for each depletion. The diagonal black lines overlaying the keogram in Figure 2 show these fits to the three depletions that they

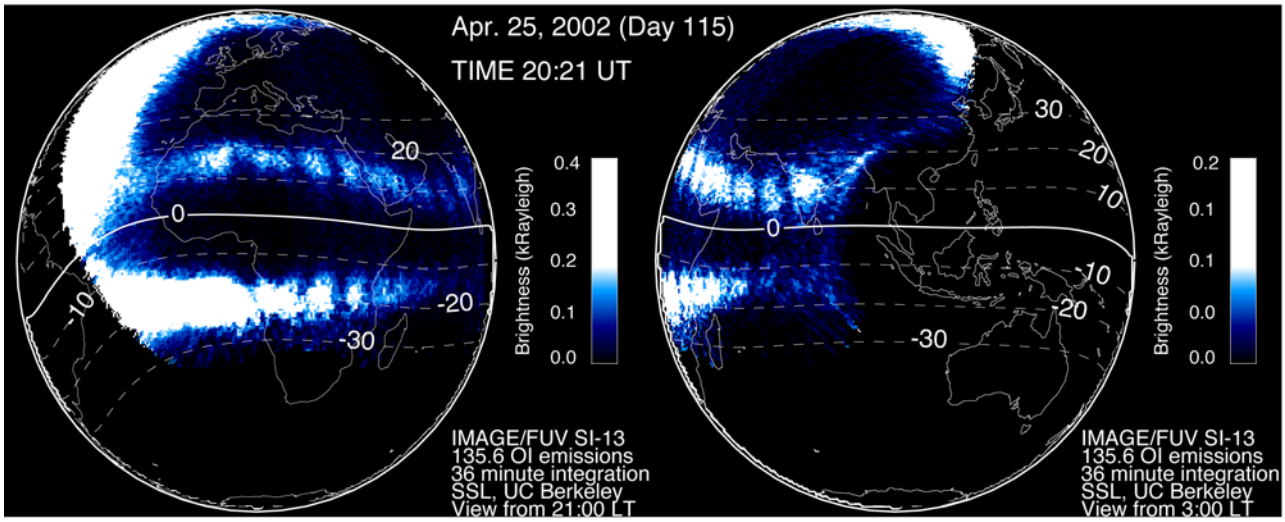

Figure 1. Ionospheric ultraviolet emissions measured by IMAGE-FUV projected onto a pair of orthographic projections of the earth, centered on 2100 and 0300 LT. A series of 19 images, each of 5 s exposure, taken across 36 min were combined in order to produce the average map of the emission brightness which is shown. Data are from 25 April 2002, from 2021 to 2057 UT. Lines of constant magnetic latitude are indicated. The bright emissions on the left side of the left image and top of the right image come from dayglow emissions from thermospheric OI. The equatorial ionospheric anomaly is visible throughout the evening as a pair of bright emission bands centered around 10–20° MLat. Ionospheric depletions are visible within both of these bands.

were able to identify for this orbit (the horizontal black line corresponds to missing spacecraft data). Taking the derivative of these polynomial fits, *Immel et al.* [2003] were able to find the depletion drift velocity. This process was repeated for each orbit from March to May 2002, producing a database of 94 depletion velocity measurements as functions of UT. This database was then used in the various studies described in section 1.

3. Tracking Of Airglow Depletions (TOAD)

[11] It is clear from Figure 2 that a number of visible depletions were missed using the technique described in section 2. These were presumably overlooked due to human time constraints. To improve on this, we have developed a fully automatic and objective procedure, that requires no human input and that also calculates velocities as a function of MLat. This procedure is referred to as Tracking Of Airglow Depletions (TOAD).

[12] Unlike in previous studies, TOAD identifies depletions in multiple keograms, each representing observations in only one half degree of MLAT. Structures in the airglow and the depletions are still visible in each keogram of an individual half degree MLat bin (not shown here), but the signal to noise ratio is relatively low compared to that shown in Figure 2. In order to increase the accuracy of the tracking

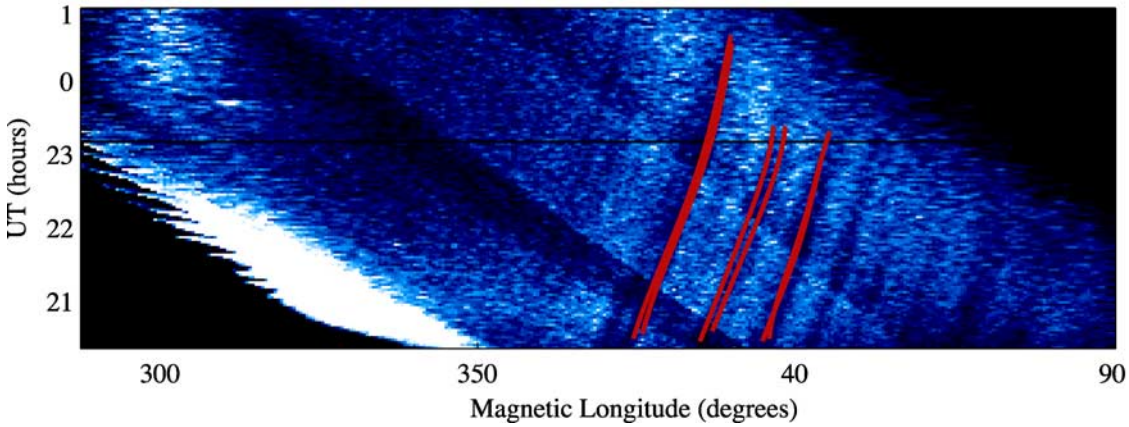

Figure 2. Keogram of the integrated 135.6 nm brightness over the northern airglow band (integrated over 0–25° MLat) observed by IMAGE-FUV for the orbit as shown in Figure 1. The depletions are seen to move eastward with UT. Overlaid on the keogram are lines showing the 4th order polynomial fits from *Immel et al.* [2003] for the three depletions they tracked in this data set. The horizontal black line around 2300 UT corresponds to missing spacecraft data.

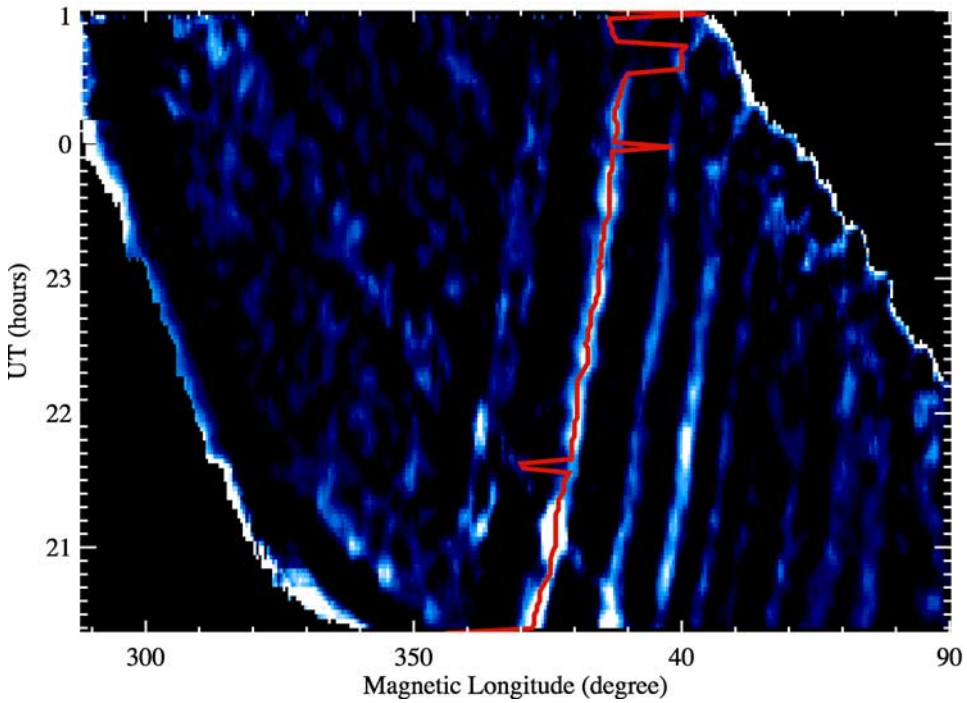

Figure 3. Keogram of the residual ionospheric variations, highlighting the depletions using the method described in the text. Data are for the same period as shown in Figure 2. Overlaid is one example track identified by TOAD at 12° MLat, prior to the application of data rejection algorithms. While the tracking routine follows the depletion well across most of its duration, at later UT when the brightness of the anomaly is significantly reduced, there are several departures which must be corrected for later, as described in the text.

program, the keogram goes through three image processing steps to highlight the depletions: (1) brightness equalization, (2) noise reduction, and (3) subtraction of medium-scale background variations.

[13] 1. It can be seen from Figure 2 that there are two dark bands, related to instrument calibration and design and also a bright band of dayglow which move westward at the velocity of the Earth's rotation. These strong features must be removed from the keogram before automated tracking of depletions can be implemented. In order to remove these, as well as the background changes in brightness with LT, we first rotate the keogram counter clockwise such that a line of constant LT is horizontal. Then each point on each row is divided by the average brightness of that row. The new keogram now represents only variations of brightness at constant LT. This is then rotated back into the original orientation.

[14] 2. In order to remove noise on a scale of less than the width of a typical depletion observed by IMAGE-FUV (around 3–5° MLon), we smooth each row of the keogram with a boxcar average with width of 2.5° MLon (the keogram used has a regularly spaced grid of half degree MLat by half degree MLon).

[15] 3. A strong medium-scale variation with MLon related to normal ionospheric density variations also exists in each keogram. These variations are of significantly larger scale than the depletions which we wish to track. To remove these medium-scale variations, we first create a copy of the keogram. This copy is then smoothed with a boxcar average of width 20° Mlon. The unaltered keogram is then subtracted from the smoothed keogram.

[16] The product of the application of these steps is shown in Figure 3. As can be seen in a comparison to Figure 2, it is now much easier to see the depletions in the keogram.

[17] The process of tracking starts from a reference point on the keogram. TOAD takes a 10° window, centered on this reference point, and finds the linear Pearson correlation coefficient of the data in this window with the data above and below this point in the keogram. In order to track the depletions similar to seen by *Immel et al.* [2003], TOAD searches rows in the keogram above and below (corresponding to later and earlier UT) in a region moving eastward through the reference position in the velocity range of 1.5–12° hr^{-1}. Using this process, TOAD finds the track of highest correlation to the reference point, both earlier and later in UT. The line overlaid on Figure 3 shows an example of one of these tracks for the 12° MLat keogram.

[18] It can be seen in Figure 3 that the line of highest correlation does not always follow the depletion. The highest correlation may be found in a neighboring depletion when two depletions are sufficiently close together or at a random position when no good correlation can be found. In order to correct for this, a confidence value is assigned to each data point on the track. This value is based on the deviation from the least squares-fitted straight line of the complete track. In addition, as the depletions are expected to move eastward and westward moving artifacts still remain in the keogram (such as edges of the data) tracks which have a net westward motion are removed.

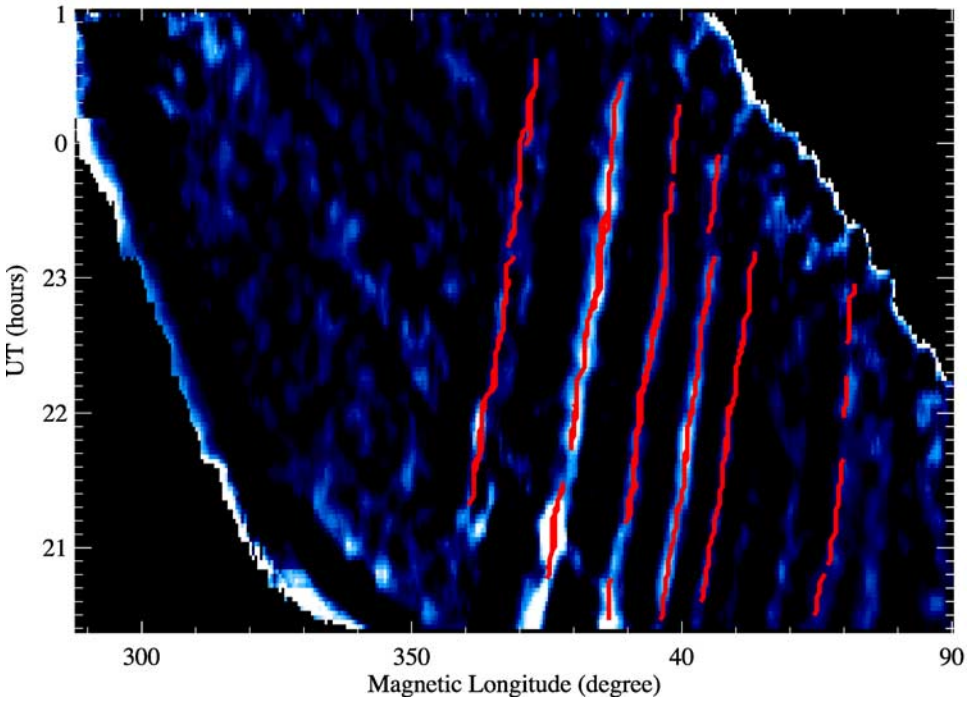

Figure 4. As Figure 3, but showing several example tracks found at 12° MLat for each of the depletions identified by TOAD for the period shown in Figure 2 after all data rejection algorithms have been applied.

[19] In order to automatically search for all depletions in the keogram, TOAD tests reference points at each half degree MLon point across the width of the keogram. Each depletion does not necessarily pass through any one line of constant UT, so the reference point must be tried on each MLon at more than one UT. However, as this process is computationally expensive, TOAD scans only three evenly spaced UT (2133 UT, 2243 UT, and 2353 UT for the example shown here). This means in this case that TOAD does not necessarily capture the depletions lasting less than 1 h and 10 min. This step does not limit the final number of depletions which TOAD is sensitive to, as shown below. This process is repeated for each MLat across the 0–25° MLat range at intervals of 0.5°. Figure 4 shows several example tracks found for the 12° MLat keogram. As can be seen, TOAD has found all major depletions visible in this keogram.

[20] Figure 4 shows the combination of a number of tracks from the three scans in UT. As can be seen, TOAD has tracked the same depletion multiple times. In order for the velocity of each depletion to be found, the tracks belonging to each individual depletion need to be gathered together from across different MLon and MLat. In order to do this, we first construct a single keogram, showing all the tracks identified by TOAD across all MLat. Next, a flood-fill algorithm is used to sweep this keogram in both MLon and UT and assign an identification number to all tracks belonging to a single depletion. As TOAD is intended to retrieve velocities across a range of MLat and MLT, this algorithm has been configured to only select the depletions which are clearly visible (have a minimum total area on the keogram) and last for a minimum of 2 h. After this process has been completed, we are left with the keogram shown in Figure 5.

[21] From Figure 5, it can be seen that TOAD has identified a total of five depletions. Comparing to Figure 2, it can be seen that depletion 1 and depletion 3 are both composed of two separate depletions, but TOAD has identified each as just one depletion. This means that TOAD miscounts the total number of depletions in any one keogram. However, this is not critical as the goal is not to determine the total number of depletions, and it is envisaged that the velocities found by TOAD will be of most use in statistical surveys. As may be expected, TOAD is less reliable at later LT because the airglow brightness falls significantly, making it difficult to discern the depletions from the background. If a cutoff LT had been used in the keogram, depletions 3a and 3b would have been identified as two separated depletions, but this was not deemed necessary for the purposes of demonstrating this technique.

[22] Each track found by TOAD contains data of the position of the depletion in MLon as a function of UT over a half degree MLat range. These data can be used to find the drift velocity as a function of UT. To do this, the positions are first smoothed using an edge-truncated boxcar average with a smoothing window equal to the length of the track. A second-order polynomial is fitted to this smoothed position data. As the position data associated with each depletion are comprised of several tens of individual tracks, the second-order fit used here does not constrain the velocity found by TOAD (the derivative of this second-order fit) for an entire depletion to be linear with UT.

[23] Using the derivative of these multiple fits, TOAD is able to calculate the mean velocity of each depletion. By holding one variable constant, these velocities can be

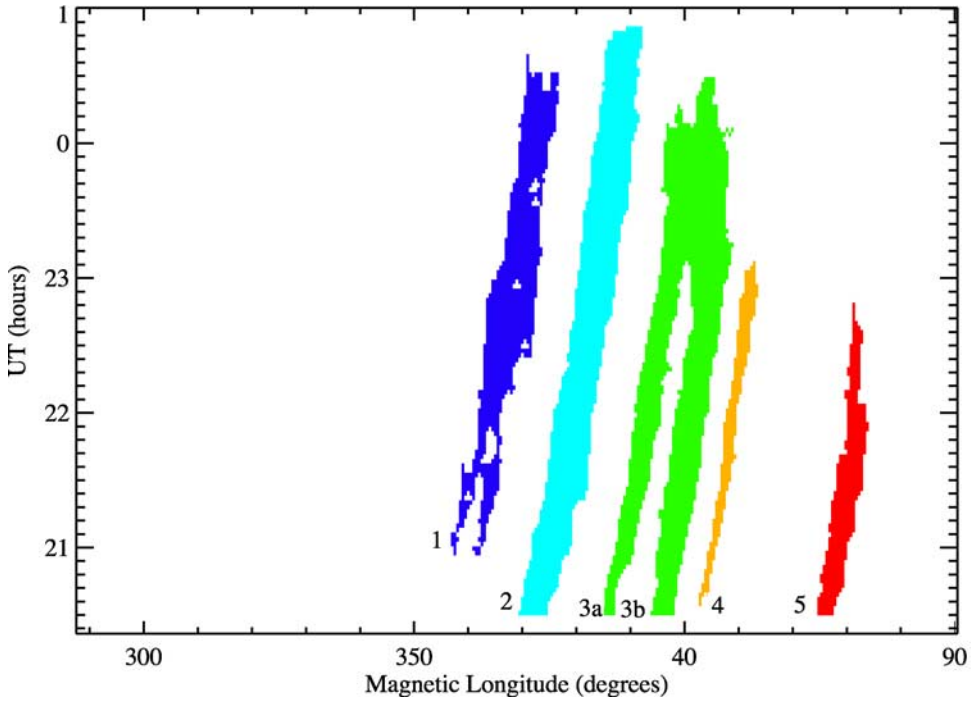

Figure 5. Keogram showing all positions tracked for each of the depletions identified by TOAD for the period shown in Figure 2 over all MLat after all data rejection algorithms have been applied. Each of the depletions has been labeled to allow easy identification in the text and later figures.

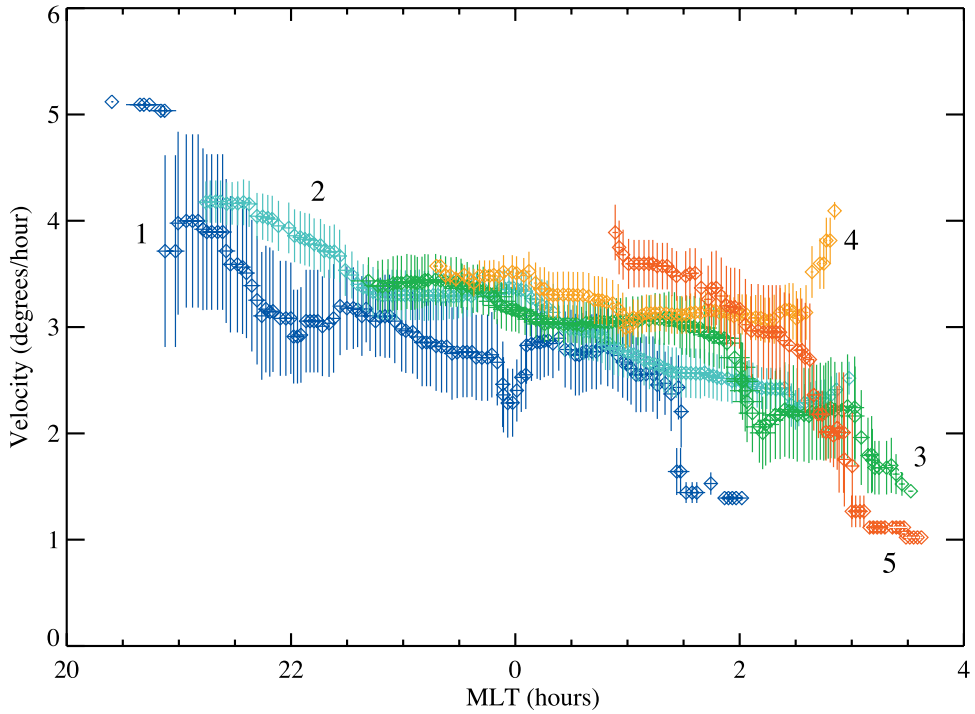

Figure 6. Mean and standard deviation of the zonal drift velocities as a function of LT for each of the depletion identified by TOAD for the period shown in Figure 2. Each of the 5 depletions are labeled to allow a comparison with Figure 5.

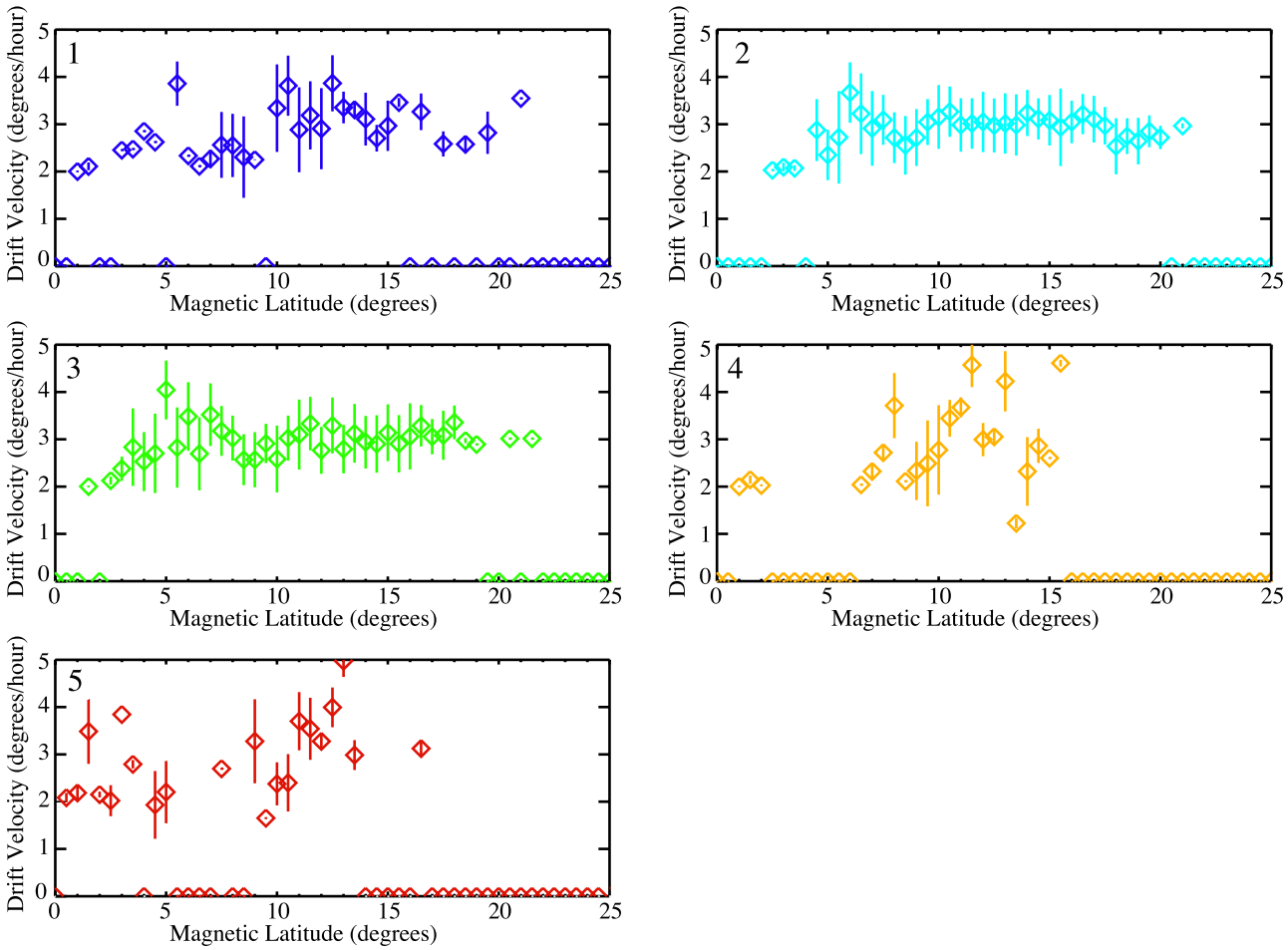

Figure 7. Mean and standard deviation of the zonal drift velocities as a function of MLat for each of the five depletions identified by TOAD for the period shown in Figure 2. Each depletion is labeled to allow a comparison with Figures 5 and 6.

plotted as a function of MLT or MLat. Figure 6 shows the mean zonal drift velocities as a function of MLT. Each depletion is labeled to allow easy comparison with Figure 5. The uncertainties shown are calculated from the spread of velocities of the different tracks, taking into account that not all tracks are independent estimates of the velocity of each depletion. Here we have assumed that there are only three unique reference windows used in the process leading up to Figure 3. These unique reference windows are at the left and right edges of the depletion and in its center. The general trend shown in Figure 6 is that the drift velocities fall steadily after 2000 MLT. It is worth noting that this result is not a statistical survey of the data but it is only that of five depletions from one orbit. We should also note here that statistics of velocities are significantly better for depletion 2 and 3 because they are the clearest depletions in the original keogram and hence a greater number of successful tracks have been recorded.

[24] Figure 7 shows the mean zonal drift velocities as a function of MLat. For the purpose of this plot, we did not subdivide the data by MLT. Because of the limited instrument count rates, TOAD is of limited reliability away from the region where the airglow is brightest. For the data considered here, the brightest airglow emissions are centered on 13° MLat, with a full width at half maximum of 10° MLat. Therefore the most reliable velocities are expected to be found in the 8–18° MLat range and for depletions 2 and 3. If we consider the drift velocities for these, Figure 7 shows that there is no significant velocity shear with MLat. However, given the limited amount of data available in this five hour observational period, subdividing these drift velocities by both MLT and MLAT simultaneously does not leave us with sufficient continuous data needed for further meaningful analysis. Therefore it is entirely possible that significant latitudinal shears may be observed at certain MLT which must be investigated more thoroughly in a statistical survey of the IMAGE-FUV data.

4. Comparison of TOAD With Previous IMAGE-FUV Analysis

[25] The results from TOAD show a significant improvement over the previous studies. Using TOAD, the number of depletions tracked is nearly doubled, the zonal drift velocities for each depletion have been found as a function of both MLT and MLat, and finally uncertainties in all measured velocities have been quantified.

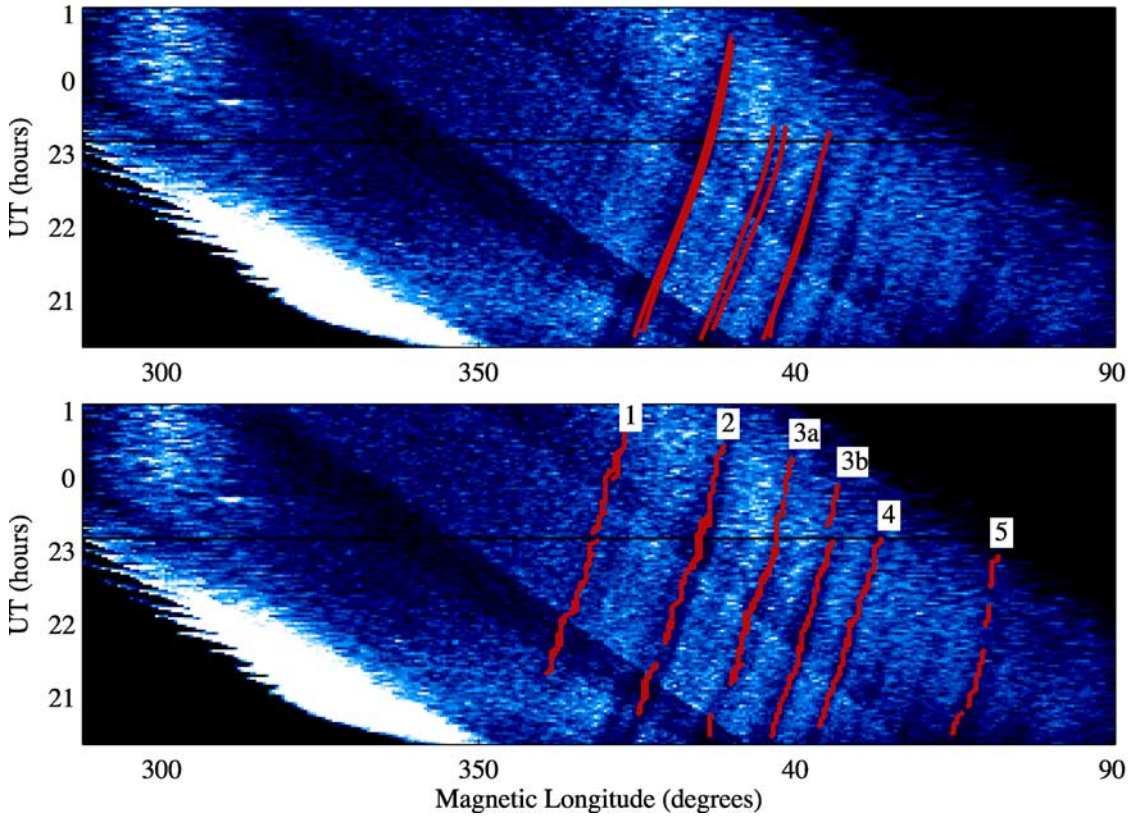

Figure 8. Comparison of tracks identified by *Immel et al.* [2003] and a number of example tracks at 12° MLat identified by TOAD for the data shown in Figure 2. The 5 depletions identified by TOAD are labeled to allow comparison with Figures 5 to 7.

[26] Figure 8 shows a comparison of the tracks identified by *Immel et al.* [2003] and the example tracks identified by TOAD at 12° MLat from Figure 4. As mentioned in the previous section, there are a number of clear depletions missing using the technique described in section 2 (identified as depletions 1, 4, and 5 in Figure 8). TOAD is able to track all of the depletions found by the previous method, as well as the three that were not tracked. It is worth noting that the two clear depletions between depletions 4 and 5 have been excluded from this study, even though they were initially captured by TOAD, because they do not last for 2 h.

[27] Owing to time constraints, *Immel et al.* [2003] did not measure the drift velocities as a function of MLat; therefore we can only compare the velocities obtained as functions of MLT. Figure 9 shows the zonal drift velocities of the three best tracks from Figure 2. The tracks are labeled to allow easy comparison with previous figures. *Immel et al.* [2003] used the derivative of a first- through fourth-order polynomial fits shown in Figure 8 in order to calculate the velocities shown here. As can be seen in Figure 8, these polynomial fits closely follow the depletions in the center of the time series but curve away from the data toward the beginning and end of each track due to the increasing dominance of highest-order coefficients. This is evident in the fits to depletions 2 and 3a at later MLT in Figure 8 and again in Figure 9, where the zonal drift velocities are seen to rapidly increase for depletion 2 from 2130 to 2300 MLT and for depletion 3b from 0130 to 0230 MLT.

[28] For the depletions shown here, we can compare the calculated velocities from the two schemes. It is evident from comparing Figures 6 and 9 that both schemes reveal an overall trend of decreasing zonal drift velocities with MLT, as may be expected from previous studies cited in section 1. However, the velocities retrieved by TOAD tend to be lower than those found by *Immel et al.* [2003]. This can most likely be attributed to differences in the order and number of the fits performed in each routine. However, as this example is not a rigorous survey of the IMAGE-FUV database, it is not possible to say if any systematic difference in the zonal drift velocities measured by each scheme exists.

[29] Further insight can be gained by considering data from 1700 to 2300 UT on 7 May 2002. During this interval, the nighttime airglow brightness was substantially lower than that considered above and it is not easily visible against the strong dayglow which appears in the standard keogram for this period. As such, *Immel et al.* [2003] found no depletions in this data. However, by altering the plotting scale from that shown in Figure 2, it is possible to pick out clear depletions in the nighttime airglow (this step was not attempted by *Immel et al.* [2003] because of human time constraints). These can be seen in Figure 10. Thanks to the brightness equalization step described in section 3, TOAD is able to identify and track four depletions in these data. The locations of these are shown in Figure 11. While the results from the analysis of such a dim time period may benefit from some level of post-TOAD human inspection for quality control purposes, the application of this method to

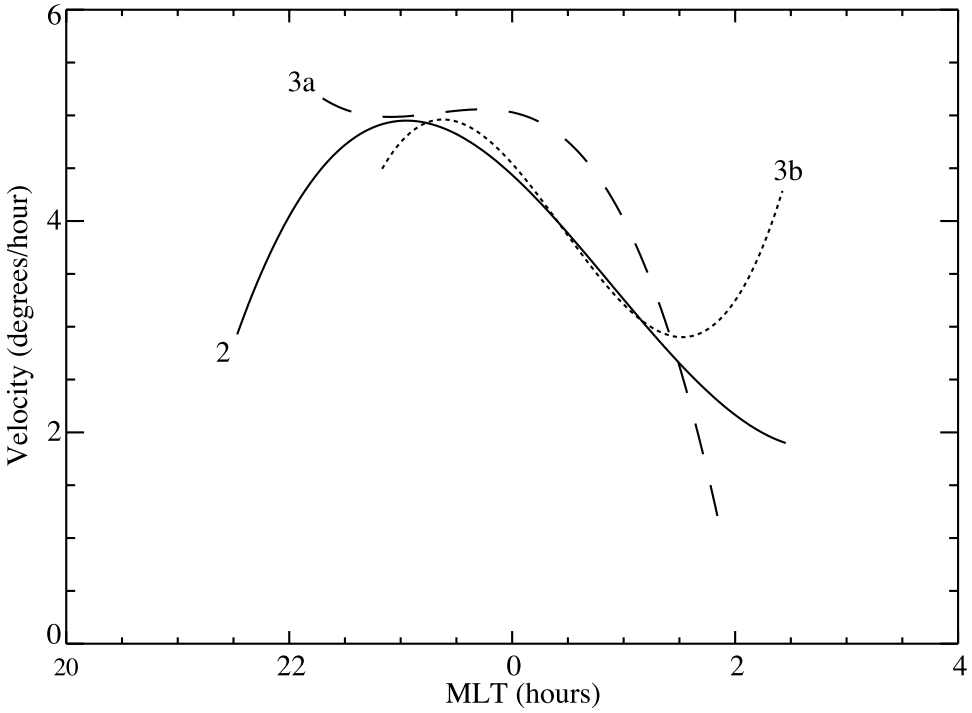

Figure 9. Zonal drift velocities determined by *Immel et al.* [2003] for the three plasma depletions highlighted in Figure 2. The solid line represents depletion 2, the dashed line represents depletion 3a, and the dotted line represents depletion 3b.

such a challenging interval of data highlights the strengths of this technique.

[30] The increased quantity of depletions tracked using TOAD without requiring any human input makes this scheme more suitable for statistical surveys of large data sets than the previous IMAGE-FUV analysis described in section 2. The ability of TOAD to track a large number of drift velocities as a function of MLat opens the possibility of studying their latitudinal shear on a global scale for the first time. Finally, as TOAD is able to identify the mean drift

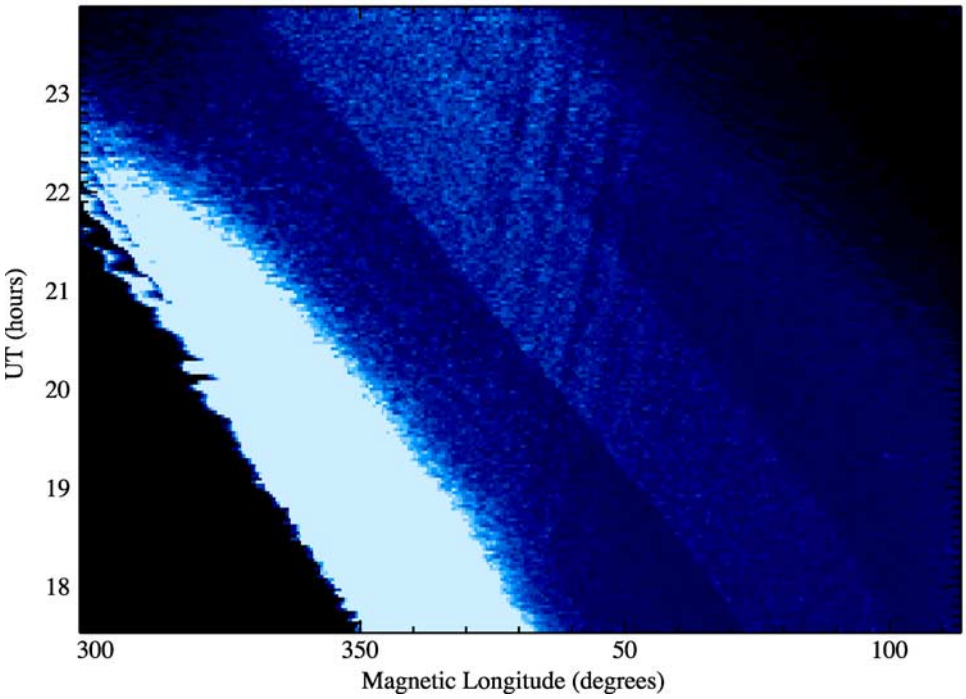

Figure 10. Keogram of the integrated UV brightness over the northern airglow band (integrated over 0–25° MLat) observed by IMAGE-FUV on the 7 May 2002.

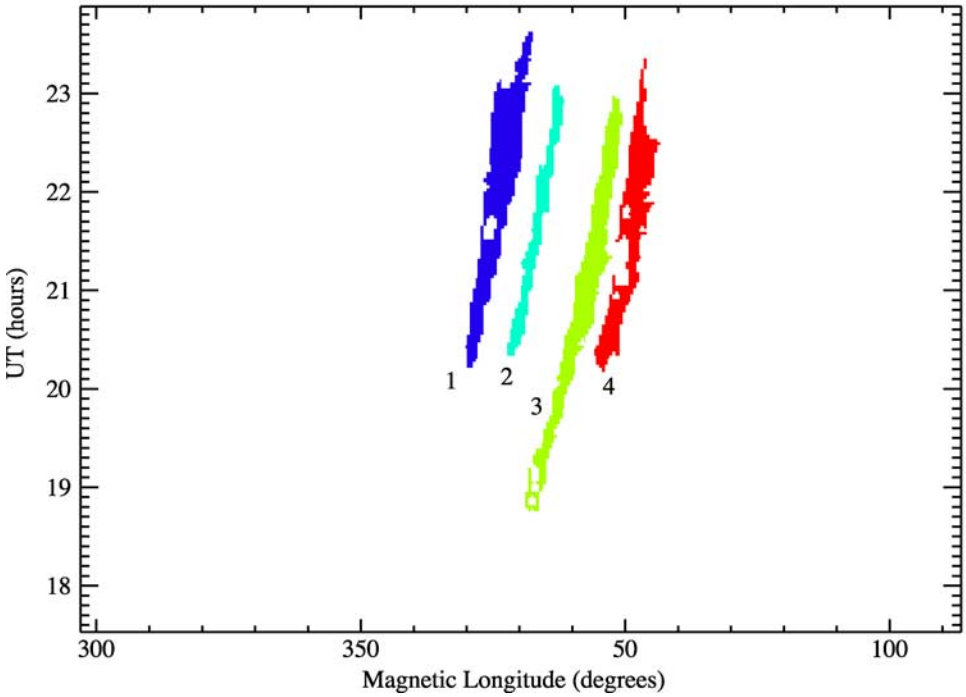

Figure 11. As Figure 5, but for the 7 May 2002.

velocity of each depletion and quantify the uncertainty in each individual estimate, this scheme also promises to be of great value in future case studies.

[31] **Acknowledgments.** IMAGE-FUV analysis is supported by NASA through Southwest Research Institute subcontract 83820 at the University of California, Berkeley, contract NAS5-96020. Additional SI-13 analyses are supported through NASA SEC Guest Investigator grants NNG04GH05G and NNG04G170G.

[32] Amitava Bhattacharjee thanks Dirk Lummerzheim for his assistance in evaluating this paper.

References

Christensen, A. B., et al. (2003), Initial observations with the Global Ultraviolet Imager (GUVI) in the NASA TIMED satellite mission, *J. Geophys. Res.*, *108*(A12), 1451, doi:10.1029/2003JA009918.

England, S. L., T. J. Immel, E. Sagawa, S. B. Henderson, M. E. Hagan, S. B. Mende, H. U. Frey, C. M. Swenson, and L. J. Paxton (2006a), Effect of atmospheric tides on the morphology of the quiet-time, postsunset equatorial ionospheric anomaly, *J. Geophys. Res.*, *111*, A10S19, doi:10.1029/2006JA011795.

England, S. L., S. Maus, T. J. Immel, and S. B. Mende (2006b), Longitudinal variation of the *E*-region electric fields caused by atmospheric tides, *Geophys. Res. Lett.*, *33*, L21105, doi:10.1029/2006GL027465.

Fejer, B. G., S. A. Gonzalez, E. R. de Paula, and R. F. Woodman (1991), Average vertical and zonal F region plasma drifts over Jicamarca, *J. Geophys. Res.*, *96*, 13,901–13,906.

Henderson, S. B., C. M. Swenson, A. B. Christensen, and L. J. Paxton (2005a), Morphology of the equatorial anomaly and equatorial plasma bubbles using image subspace analysis of Global Ultraviolet Imager data, *J. Geophys. Res.*, *110*, A11306, doi:10.1029/2005JA011080.

Henderson, S. B., C. M. Swenson, J. H. Gunther, A. B. Christensen, and L. J. Paxton (2005b), Method for characterization of the equatorial anomaly using image subspace analysis of Global Ultraviolet Imager data, *J. Geophys. Res.*, *110*, A08308, doi:10.1029/2004JA010830.

Humm, D. C. (1998), Design and performance of the Global Ultraviolet Imager (GUVI), in *EUV, X-Ray, and Gamma-Ray Instrumentation for Astronomy IX*, edited by O. H. Siegmund and M. A. Gummin, *Proc. SPIE*, *3445*, 2–12.

Immel, T. J., S. B. Mende, H. U. Frey, L. M. Peticolas, and E. Sagawa (2003), Determination of low latitude plasma drift speeds from FUV images, *Geophys. Res. Lett.*, *30*(18), 1945, doi:10.1029/2003GL017573.

Immel, T., H. Frey, S. Mende, and E. Sagawa (2004), Global observations of the zonal drift speed of equatorial ionospheric plasma bubbles, *Ann. Geophys.*, *22*, 3099–3107.

Immel, T. J., E. Sagawa, S. L. England, S. B. Henderson, M. E. Hagan, S. B. Mende, H. U. Frey, C. M. Swenson, and L. J. Paxton (2006), Control of equatorial ionospheric morphology by atmospheric tides, *Geophys. Res. Lett.*, *33*, L15108, doi:10.1029/2006GL026161.

Lin, C. S., T. J. Immel, H.-C. Yeh, S. B. Mende, and J. L. Burch (2005), Simultaneous observations of equatorial plasma depletion by IMAGE and ROCSAT-1 satellites, *J. Geophys. Res.*, *110*, A06304, doi:10.1029/2004JA010774.

Meier, R. R. (1991), Ultraviolet spectroscopy and remote sensing of the upper atmosphere, *Space Sci. Rev.*, *58*, 1–185.

Mende, S. B., et al. (2000a), Far ultraviolet imaging from the IMAGE spacecraft. 1. Systems design, *Space Sci. Rev.*, *91*, 243–270.

Mende, S. B., et al. (2000b), Far ultraviolet imaging from the IMAGE spacecraft. 3. Spectral imaging of Lyman-α and OI 135.6 nm, *Space Sci. Rev.*, *91*, 287–318.

Paxton, L. J. (1999), Global ultraviolet imager (GUVI): measuring composition and energy inputs for the NASA Thermosphere Ionosphere Mesosphere Energetics and Dynamics (TIMED) mission, in *Optical Spectroscopic Techniques and Instrumentation for Atmospheric and Space Research III*, edited by A. M. Larar, *Proc. SPIE*, *3756*, 265–276.

Richmond, A. D. (1995), Ionospheric electrodynamics using magnetic apex coordinates, *J. Geomagn. Geoelectr.*, *47*, 191–212.

Sagawa, E., T. Maruyama, T. J. Immel, H. U. Frey, and S. B. Mende (2003), Global view of the nighttime low-latitude ionosphere by the IMAGE/FUV 135.6 nm observations, *Geophys. Res. Lett.*, *30*(10), 1534, doi:10.1029/2003GL017140.

Sagawa, E., T. J. Immel, H. U. Frey, and S. B. Mende (2005), Longitudinal structure of the equatorial anomaly in the nighttime ionosphere observed by IMAGE/FUV, *J. Geophys. Res.*, *110*, A11302, doi:10.1029/2004JA010848.

S. L. England, H. U. Frey, T. J. Immel, S. B. Mende, and S. H. Park, Space Sciences Laboratory, University of California, Berkeley, Berkeley, CA 94720, USA. (england@ssl.berkeley.edu)